IMPACT OF LIVER-SPECIFIC SURVIVAL MOTOR NEURON (SMN) DEPLETION ON PERIPHERAL AND CENTRAL NERVOUS SYSTEM TISSUE PATHOLOGY

Monique Marylin Alves de Almeida[1,2], Yves De Repentigny[1], Sabrina Gagnon[1], Emma R. Sutton[1,2], Rashmi Kothary[1,2,3,4*]

[1]Regenerative Medicine Program, Ottawa Hospital Research Institute, Ottawa, K1H 8L6, Canada
[2]Centre for Neuromuscular Disease, University of Ottawa, K1H 8M5, Canada
[3]Department of Cellular and Molecular Medicine, University of Ottawa, Ottawa, K1H 8M5, Canada
[4]Department of Medicine, University of Ottawa, Ottawa, K1H 8M5, Canada
*Corresponding author: rkothary@ohri.ca

Abstract

Spinal muscular atrophy (SMA) is an inherited neuromuscular disorder stemming from deletions or mutations in the Survival Motor Neuron 1 (*SMN1*) gene, leading to decreased levels of SMN protein, and subsequent motor neuron death and muscle atrophy. While traditionally viewed as a disorder predominantly affecting motor neurons, recent research suggests the involvement of various peripheral organs in SMA pathology. Notably, the liver has emerged as a significant focus due to the observed fatty liver phenotype and dysfunction in both SMA mouse models and SMA patients. Despite these findings, it remains unclear whether intrinsic depletion of SMN protein in the liver contributes to pathology in the peripheral or central nervous systems. To address this knowledge gap, we developed a mouse model with a liver-specific depletion of SMN by utilizing an *Alb-Cre* transgene together with one Smn^{2B} allele and one *Smn* exon 7 allele flanked by loxP sites. We evaluated phenotypic changes in these mice at postnatal day 19 (P19), a time when the severe model of SMA, the $Smn^{2B/-}$ mice, typically exhibit many symptoms of the disease. Our findings indicate that liver-specific SMN depletion does not induce motor neuron death, neuromuscular pathology or muscle atrophy, characteristics typically observed in the $Smn^{2B/-}$ mouse at P19. However, mild liver steatosis was observed at this time point, although no changes in liver function were detected. Notably, pancreatic alterations resembled that of $Smn^{2B/-}$mice, with a decrease in insulin producing alpha-cells and an increase in glucagon producing beta-cells, accompanied with a reduction in blood glucose levels. While the mosaic pattern of the Cre-mediated excision precludes definitive conclusions regarding the contribution of liver-specific SMN depletion to overall tissue pathology, our findings highlight an intricate connection between liver function and pancreatic abnormalities in SMA, adding a nuanced layer to our understanding of the disease's complexities.

Keywords
Spinal muscular atrophy, neuromuscular disease, metabolism, pancreas

1. Introduction

Insufficient levels of Survival Motor Neuron (SMN) protein, primarily arising from mutations or deletions in the *SMN1* gene, are the root cause of spinal muscular atrophy (SMA), a hereditary neuromuscular disorder widely acknowledged as one of the leading genetic causes of infant mortality[1-3]. Characterized by the loss of motor neurons, SMA presents as a progressive weakening

of muscle strength, primarily impacting proximal muscles. If left untreated, this deterioration culminates in respiratory failure and premature mortality[4].

The diverse phenotypes observed in SMA patients can be attributed to the genetic variations within the *SMN* gene[1]. Humans harbor two copies of the *SMN* gene, *SMN1* and *SMN2*, which share a nearly identical sequence except for a critical C to T substitution at position 6 of exon 7 in *SMN2*[5]. This single nucleotide change disrupts splicing of the gene, resulting in the predominant production of an unstable protein lacking exon 7, known as *SMNΔ7*[5]. Despite this, approximately 10% of functional full-length (FL) SMN protein is still produced by the *SMN2* gene[2]. Consequently, the *SMN2* gene serves as a modifier of disease phenotype, with a higher copy number correlating with milder disease severity[6]. In contrast, mice possess a single copy of the *Smn* gene[2]. Notably, while homozygous deletion of both *SMN* genes has not been observed in humans, the homozygous deletion of the *Smn* gene in mice induces morphological alterations and degenerative changes in embryos post-morula stage, ultimately resulting in death at preimplantation stage[7]. This underscores the pivotal role of the *SMN* gene in early embryonic development[8].

Recent research has unveiled the extensive impact of SMN depletion beyond motor neurons, implicating additional tissues such as the liver and pancreas in both SMA patients and mouse models of SMA[9-12]. Despite major therapeutic advancements focusing on restoring SMN levels, which have notably enhanced both lifespan and quality of life in SMA patients, complete phenotypic rescue remains elusive[4,13,14]. Additionally, existing therapies primarily target postnatal treatment, potentially overlooking crucial developmental changes stemming from SMN depletion. This underscores the likelihood of a broader role for the *SMN* gene in multiple non-neuronal cell types, necessitating further exploration.

Attention has been increasingly drawn to the liver as a critical area of investigation in SMA research. Both clinical studies and preclinical mouse models have unveiled disruptions in fatty acid metabolism, leading to an increased susceptibility among SMA patients to dyslipidemia and liver steatosis[12,15-18]. Given its multifaceted role in regulating numerous biological functions, including the storage and regulation of lipids, carbohydrates, amino acids, and iron, as well as the synthesis of essential growth factors and the clearance of toxic metabolites, any disruptions in liver function may have deleterious effects on other tissues[19].

To explore the role of SMN in the liver, prior studies have utilized a transgenic mouse model featuring the Cre recombinase transgene driven by the α-fetoprotein promoter (*Alfp-Cre*). This approach led to near-total depletion of SMN protein specifically in the liver, resulting in severe impairment of liver development and late embryonic lethality[8]. In our study, to better represent the level of SMN depletion in the liver observed in SMA and elucidate the intricate interplay between SMN deficiency in the liver and its systemic impact in SMA-like pathology, we utilized a mouse model employing *Alb-Cre*, where the albumin promoter drives expression of Cre recombinase in a liver-specific manner. This model also harbors one Smn^{2B} allele and one *Smn* exon 7 allele flanked by loxP sites. The Smn^{2B} allele contains a 3-base pair substitution in the mouse *Smn* gene, resulting in aberrant splicing of exon 7[20,21]. Consequently, this genetic approach results in the production of approximately 30% full-length functional SMN protein production in the liver.

Our findings reveal that our novel liver specific SMN depleted (herein referred to as *Alb*$^{Cre/+}$;*Smn*$^{2B/F7}$) mouse model induces mild liver steatosis and disrupts pancreatic function, characterized by decreased insulin-positive and increased glucagon-positive cells, alongside reduced blood glucose levels. Remarkably, this mouse model does not exhibit an overt SMA phenotype, demonstrating normal lifespan and motor function. Nevertheless, our data suggests an intricate relationship between hepatic function and pancreatic abnormalities in SMA, thereby enhancing our comprehension of the disease's pathophysiology.

2. Results

2.1 Generation of liver-specific SMN-depleted mice

To elucidate the impact of liver specific SMN depletion on both CNS and peripheral tissue pathology, we utilized mice expressing Cre recombinase under the control of the mouse albumin promoter, referred to as *Alb*^{Cre}. This strain is commonly employed for liver-specific gene knockout using the Cre/loxP system[22]. We generated the *Smn*$^{2B/F7}$ genotype by crossing *Smn*$^{F7/F7}$ with *Smn*$^{2B/2B}$ mice (Fig. 1A). The *Smn*$^{2B/F7}$ genotype carries one allele harboring a three nucleotide switch in the exon splicing enhancer within exon 7 of the mouse *Smn* gene (known as *Smn*^{2B} allele), mimicking the *SMN2* gene in humans[21], while the other allele features exon 7 flanked by l*oxP* sites[23]. Additionally, crosses between *Alb*^{Cre} and *Smn*$^{F7/F7}$ yielded *Alb*$^{Cre/+}$;*Smn*$^{F7/+}$ offspring.

The liver-specific mouse line was subsequentially established through further genetic crosses between *Alb*$^{Cre/+}$;*Smn*$^{F7/+}$ and *Smn*$^{2B/F7}$, resulting in various genotypes, including +/+;*Smn*$^{2B/F7}$ (Fig. 1B), and *Alb*$^{Cre/+}$;*Smn*$^{2B/F7}$ (Fig. 1C). As +/+;*Smn*$^{2B/F7}$ mice lack Cre recombinase, they were used as heterozygous controls. In contrast, recombination occurs in *Alb*$^{Cre/+}$;*Smn*$^{2B/F7}$ animals resulting in the specific deletion of one allele of exon 7 in the liver, while the *Smn*2B allele remains unaffected.

Smn$^{2B/-}$ mice express approximately 15% residual full-length SMN[24] (FLSMN) compared to *Smn*$^{2B/+}$ heterozygous mice. Therefore, both genotypes were included in this study as additional controls. Tissues were collected at postnatal day 19 (P19), corresponding to the symptomatic phase of the *Smn*$^{2B/-}$ mouse model. At this stage, *Smn*$^{2B/-}$ mice show increased liver steatosis and metabolic defects, ultimately culminating in multiple system defects and mortality, typically occurring around P25[25].

We first assessed SMN protein levels in the liver and across CNS and peripheral tissues. Our findings confirmed a reduction in SMN protein levels across various tissues in *Smn*$^{2B/-}$ mice (Fig. 2A-E). However, in *Alb*$^{Cre/+}$;*Smn*$^{2B/F7}$, there was a ~70% decrease in FLSMN protein expression in the liver (Fig. 2A, A') compared to littermate control counterparts (+/+;*Smn*$^{2B/F7}$). Conversely, SMN protein levels in the brain (Fig. 2B, B'), muscle (Fig. 2C, C'), SC (Fig. 2D, D') and pancreas (Fig. 2E, E') remained unaltered, indicating that deletion of *Smn* exon 7 was restricted to the liver in *Alb*$^{Cre/+}$;*Smn*$^{2B/F7}$mice.

2.2 Alb$^{Cre/+}$;*Smn*$^{2B/F7}$ *mice show mild yet important liver steatosis*

131 We previously showed that *Smn*$^{2B/-}$ mice exhibit defects in fatty acid metabolism and lipid
132 accumulation in the liver[12,16-18]. Additionally, SMA patients face an elevated risk of dyslipidemia
133 and steatosis[12]. Hence, we explored whether the intrinsic decrease in SMN levels restricted to the
134 liver would lead to increased lipid accumulation. Histology from *Alb*$^{Cre/+}$*;Smn*$^{2B/F7}$ mice (Fig. 3A)
135 qualitatively indicates some level of hepatic microvesicular steatosis and lipid accumulation.
136 However, there was a noticeable variation in cell morphology and Oil Red-O retention among
137 hepatocytes, suggesting incomplete recombination.

138 Consistent with the histological findings, *Alb*$^{Cre/+}$*;Smn*$^{2B/F7}$ mice showed variable triglycerides
139 levels (n1=45.95, n2=10.10; n3=75.72; n4=21.91 μg/mg, mean±SEM 38.44±14.48) (Fig. 3B), and
140 yet higher than those observed in +/+;*Smn*$^{2B/F7}$ controls (n1=2.60, n2=0.15; n3=0.66; n4=1.44
141 μg/mg, mean±SEM 1.213±0.5332), although this difference did not reach statistical significance
142 (p=0.0824). As expected, *Smn*$^{2B/-}$ controls exhibited increased lipid accumulation and triglyceride
143 levels. Taken together, the data suggest an intrinsic role of SMN in regulating fat liver metabolism.

144 *2.3 Liver-specific SMN depletion does not perturb liver homeostatic function*
145
146 We next sought to identify whether *Alb*$^{Cre/+}$*;Smn*$^{2B/F7}$ mice display disturbed liver homeostatic
147 function. Specifically, we evaluated parameters associated with iron metabolism (Fig. 4A,B),
148 endoplasmic reticulum (ER) stress (Fig. 4C), and insulin-like growth factor (IGF-1) (Fig. 4D)
149 levels, all of which have previously been identified as altered in *Smn*$^{2B/-}$ mice[18] and were further
150 confirmed in our study. Our analysis revealed no significant differences in the protein levels of
151 heme oxygenase, transferrin, P62, and IGF-1 between the *Alb*$^{Cre/+}$*;Smn*$^{2B/F7}$ and +/+*;Smn*$^{2B/F7}$
152 control groups. These findings suggest that liver-specific SMN depletion may not play a significant
153 role in these pathways or that the mosaic nature of Cre-mediated excision resulted in a partial effect
154 that was difficult to pick up at this time point.
155

156 *2.4 Liver-specific SMN depleted mice display pancreatic defects*
157
158 We have demonstrated pancreatic and glucose abnormalities in the *Smn*$^{2B/-}$ mouse model of SMA
159 and type I SMA patients[11,26]. Therefore, we conducted immunohistochemistry to investigate the
160 cellular profile of the pancreas, aiming to ascertain whether the targeted depletion of SMN in the
161 liver contributes to pancreatic dysfunction. Surprisingly, double-labeling of insulin-producing β
162 cells and glucagon-producing α cells revealed a significant decrease in the proportion of β cells
163 and a notable increase in α cells in the pancreas of *Alb*$^{Cre/+}$*;Smn*$^{2B/F7}$ mice compared to
164 +/+*;Smn*$^{2B/F7}$ and *Smn*$^{2B/+}$ heterozygous controls (Fig. 5A-C). This loss of β cells and rise in α cells
165 could suggest a functional impairment in glucose metabolism. Consequently, we evaluated non-
166 fasting glucose levels in these mice (Fig. 5D), revealing reduced blood glucose levels in
167 *Alb*$^{Cre/+}$*;Smn*$^{2B/F7}$ mice relative to +/+*;Smn*$^{2B/F7}$ and *Smn*$^{2B/+}$. However, blood glucose levels
168 remained higher than those observed in *Smn*$^{2B/-}$ mice. Overall, these findings indicate imbalances
169 in α and β cell fate within pancreatic islets in *Alb*$^{Cre/+}$*;Smn*$^{2B/F7}$ mice, resembling those observed in
170 *Smn*$^{2B/-}$ mice. Furthermore, the maintenance of SMN protein expression at levels comparable to
171 those of heterozygous controls in the pancreas (Fig. 2E,E') suggests that selective SMN depletion
172 in the liver may be implicated in the dysfunction of the pancreas-liver axis.

2.5 Motor neurons, neuromuscular junction (NMJ) or motor fibers are unaffected in liver specific SMN depleted mice

The hallmark features of SMA include the degeneration of lower spinal motor neurons, neuromuscular junction (NMJ) pathology, and muscle atrophy[10,25,27-33]. While the exact mechanisms linking these changes in the motor unit to the clinical manifestations of SMA remain unclear, diminished levels of SMN protein are recognized as a pivotal factor[1,2,25,33-35]. Thus, we investigated the impact of liver-specific SMN depletion on these SMA-like features. Our findings show no significant differences in motor neuron cell body counts (Fig. 6A,B), neurofilament accumulation at NMJs (Fig. 7A,B), NMJ endplate occupancy (Fig. 7A,C), muscle fiber size (Fig. 8A,B), or muscle fiber frequency distribution (Fig. 8C) among $Alb^{Cre/+};Smn^{2B/F7}$ and $+/+;Smn^{2B/F7}$ and $Smn^{2B/+}$ heterozygous controls. However, as anticipated, $Smn^{2B/-}$ mice exhibited motor neuron loss, NMJ defects, and muscle atrophy.

2.6 Liver-specific SMN depleted mice have normal survival rate and motor function

We also conducted a comprehensive assessment of survival, weight, and motor function in $Alb^{Cre/+};Smn^{2B/F7}$ and $+/+;Smn^{2B/F7}$ mice over a 60-day period (Fig. 9A). While the $Smn^{2B/-}$ mice typically have a mean survival of 25 days[25], both $Alb^{Cre/+};Smn^{2B/F7}$ and $+/+;Smn^{2B/F7}$ mice in our study survived up to 60 days (Fig. 9B), after which they were euthanized for tissue collection. Moreover, throughout the observation period, mice from both groups exhibited similar weight gain trends (Fig. 9C).

To further evaluate motor function at different stages, we implemented several age-specific behavioral tests commonly used to assess motor function[36] (Fig. 9D-F). We previously showed $Smn^{2B/-}$ mice have reduced motor function scores, as seen through increased time to right, prolonged balancing time and diminished muscle strength[26]. Here, we found no alterations in $Alb^{Cre/+};Smn^{2B/F7}$ compared to $+/+;Smn^{2B/F7}$ mice in time to right, as assessed by the righting reflex (Fig. 9D), nor in distal muscle strength measured through the inverted mesh grip test (Fig. 9E), or motor balance and coordination evaluated by the pen test (Fig. 9F). Overall, these findings collectively demonstrate that liver-specific SMN depletion does not impact survival, weight gain, or motor function.

3. Discussion

The liver is pivotal in regulating numerous biological functions in the body. These encompass, among others, the storage and balance of lipids, carbohydrates, and iron, as well as the synthesis of vital growth factors and the clearance of non-essential or harmful metabolites[19]. Given its multifaceted role, any alterations in liver function can potentially have cascading effects on other organs within the body. Hence, aside from elucidating the impact of liver specific SMN depletion on hepatic function, it is imperative to explore its effects on other tissues, as alterations in these tissues have been documented in various mouse models of SMA[11,18,34,37].

Previous work on conditional knockout of *Smn* in the livers of mice resulted in severe impairment of liver development characterized by iron overload and subsequent liver atrophy, ultimately leading to late embryonic lethality[8]. In our study, we generated a novel mouse model where instead

of a complete knockout of *Smn* in the liver, we created a scenario where SMN protein was depleted to 30% of full-length SMN production specifically within the liver, while SMN protein levels in other tissues remain comparable to those of heterozygous controls. Notably, this mouse line did not exhibit any signs of developmental delays, liver atrophy, or reduced lifespan. Nonetheless, within 19 days after birth, $Alb^{Cre/+};Smn^{2B/F7}$ mice showed a mild yet rapid onset of fatty liver disease and trends towards an increase in lipid levels when maintained on a normal chow diet, underscoring the importance of SMN in lipid metabolism.

Mild liver steatosis may be accompanied by disruptions in crucial liver function markers, notably those implicated in iron metabolism, autophagy, and growth factor regulation, such as IGF-1[18]. Accordingly, we initially investigated the expression of HO-1, an enzyme responsible for heme degradation into iron, carbon monoxide, and biliverdin; and transferrin, a liver-synthesized glycoprotein involved in iron transport across tissues (reviewed in[38]). Prior studies have documented alterations in these proteins in $Smn^{2B/-}$ mouse livers[18]. While our current analysis did not reveal significant differences in $Alb^{Cre/+};Smn^{2B/F7}$ mice, the observed upward trend in transferrin and HO levels suggests ongoing changes in iron metabolism, which may not be fully manifested at P19. In addition, incomplete Cre-mediated excision of Smn^{F7} allele may be hindering a comprehensive understanding of SMN's role in liver function.

Furthermore, no alterations were observed for P62 levels, a multifunctional scaffold protein implicated in autophagy, formation of hepatic inclusion bodies, and hepatocyte cell death (reviewed in[39]) despite its increased presence in mouse models of SMA[18]. Similarly, there were no changes detected in IGF-1 protein levels, whose deficiency has been linked to liver pathology and non-alcoholic fatty liver disease (NAFLD)[40,41], and its decrease is evident in $Smn^{2B/-}$ mice[18].

Altogether, our findings underscore the necessity of conducting further investigations at later time points to unveil potential modifications in other pathways and their repercussions on liver physiology. Additionally, the variability in the data may be due to differences in Cre recombination efficiency from mouse to mouse due to inconsistent Cre recombination among littermates, or the absence of Cre expression in certain cells leading to recombination failure[42].

Previously, our research unveiled metabolic abnormalities in SMA-like mice, including glucose intolerance, insulin hypersensitivity, and hyperglucagonemia, accompanied by changes in pancreatic islet composition characterized by an increase in glucagon-producing α-cells at the expense of insulin-producing β-cells[11]. Histopathological examination of pancreatic tissue from infants and children with SMA type I corroborated these findings, revealing a predominant presence of glucagon-producing α-cells within pancreatic islets[11]. Furthermore, one-year-old $Smn^{+/-}$mice producing approximately 50% of SMN protein, when exposed to a high-fat diet, exhibited dysregulation in the proportion of glucagon-producing α-cells within pancreatic islets and heightened hepatic insulin and glucagon sensitivity[9]. Our study uncovers a novel intrinsic role of liver-specific SMN in pancreatic function, distinct from IGF-1 signaling, pancreatic SMN levels (which remained stable), or canonical SMA pathology.

In addition, while the hallmark pathological features of SMA include motor neuron loss, NMJ pathology, muscle atrophy, and consequent motor function alterations[2,30,33-35], these were not evident in the $Alb^{Cre/+};Smn^{2B/F7}$ mouse model at P19. However, given that glucose metabolism defects are observed in various neurodegenerative and neuromuscular disorders, subsequent time

points are crucial to discern whether additional alterations arise as the mice age. Although hepatic and pancreatic abnormalities likely occur independently of disease onset, given that SMN depletion in motor neurons and muscle alone[23,43,44] is sufficient to induce a SMA-like phenotype, the potential influence of these anomalies on SMA progression warrants careful consideration.

Overall, our findings suggest that alterations in SMN production solely within the liver may suffice to induce pathological hepatic and pancreatic function, shedding light on a novel role of SMN in liver physiology.

4. **Material and Methods**

4.1 Mouse models

The *Smn*^{2B} mouse, which harbors the *Smn*^{2B} mutation resulting from the substitution of three nucleotides within the exon splicing enhancer of exon 7, was developed and maintained on a C57BL/6 background in our laboratory[21]. The FVB.129(B6)-*Smn1*^{tm1Jme} (*Smn*$^{F7/F7}$) and B6.Cg-*Speer6-ps1*$^{Tg(Alb\text{-}Cre)21Mgn}$/J (*Alb*^{Cre}) mice were acquired from The Jackson Laboratory. Liver-specific SMN-depleted mice were obtained through successive crosses between *Alb*$^{Cre/+}$;*Smn*$^{F7/+}$ and *Smn*$^{2B/F7}$ mice (see Fig. 1). Line validation was conducted via genotyping of DNA extracted from mouse ear biopsies using PCR (see Table 1 for list of primers used). Both male and female mice were included in the studies. All mice were bred and housed in the University of Ottawa Animal Facility under protocol OHRI-3343, adhering to guidelines established by the Canadian Council on Animal Care. Additionally, we employed *Smn*$^{2B/-}$ mice (a severe SMA mouse model) and asymptomatic heterozygous *Smn*$^{2B/+}$ mice as controls in our experiments.

Table 1. List of primers used for genotyping

NAME	SEQUENCE (5'-3')
Alb-Cre	TGCAAACATCACATGCACAC
	TTGGCCCCTTACCATAACTG
	GAAGCAGAAGCTTAGGAAGATGG
SmnF7	AGAAGGAAAGTGCTCACATACAAATT
	TGTCTATAATCCTCATGCTATGGAG
Smn2B	GGTTTCAGACAAAATAAAAAAGAATTTAAG
	TTTGGCAGACTTTAGCAGGGC

4.2 Tissue harvesting and processing

Following euthanasia, liver, and *tibialis anterior* (TA) muscles underwent fixation in a 1:10 dilution of buffered formalin for 48 h at 4°C, followed by transfer to 70% ethanol at the same temperature until processing. The pancreas was fixed in 4% paraformaldehyde (PFA) for 48 h at 4°C, then similarly moved to 70% ethanol for processing. For the lumbar spinal cord (SC) and liver (for Oil Red-O staining), fixation was performed overnight at 4°C in 4% PFA, followed by immersion in 30% sucrose in PBS. Subsequently, the liver and SC were flash-frozen in optimal cutting temperature (OCT) embedding medium. Cryosections of the lumbar spinal cord were cut at a thickness of 16 µm, while liver sections were cut at 10 µm and stored at -80°C until immunohistochemical analysis.

The abdominal musculature was dissected and fixed in 4% PFA for 15 min at room temperature, followed by 3 washes in 1X PBS, after which the transversus abdominis (TVA) muscle was dissected from the abdominal musculature. TA, liver, and pancreas samples were handled at the University of Ottawa Department of Pathology and Laboratory Medicine. Paraffin blocks containing tissues were sectioned at 4 μm thickness using a microtome. Sections of TA and liver were stained with hematoxylin and eosin (H&E) using an XL CV5030 autostainer from Leica. Liver cryosections were stained with Oil Red-O and counterstained with hematoxylin using established protocols. Images of H&E and Oil Red-O-stained samples were scanned with a MIRAX MIDI digital slide scanner manufactured by Zeiss. Image acquisition was performed using Panoramic Viewer 1.15.4 software.

4.3 Immunoblotting

Total protein was extracted by homogenizing flash-frozen samples of spinal cord, brain, liver, pancreas and hindlimb muscles using RIPA lysis buffer (Cell Signaling), supplemented with phenylmethylsulfonyl fluoride (PMSF, Cell Signaling). The concentrations of the extracted proteins were determined using the Pierce BCA Protein Assay kit (ThermoFisher).

For liver, brain, and spinal cord tissues, 20 μg of protein per sample were separated by 10% sodium dodecyl sulfate polyacrylamide gel electrophoresis (SDS-PAGE), while 30 μg were used for pancreas and muscle samples. Following electrophoresis, the proteins were transferred onto a PVDF membrane (Immobilon-P, Millipore) and blocked for 30 min at room temperature using intercept blocking buffer (LI-COR). Subsequently, the membranes were incubated overnight at 4°C with primary antibodies.

After incubation, the membranes were rinsed with tris-buffered saline containing 0.1% Tween-20 (TBS-T) and then incubated for 1 h at room temperature with IRDye 680R or 800CW (LI-COR) secondary antibody. Fluorescent signals were detected using the Odyssey Infrared Imaging System (LI-COR). Total raw values were normalized to α-tubulin (housekeeping protein) obtained from the same blot.

4.4 Immunohistochemistry

4.4.1 Pancreas

Pancreatic sections underwent deparaffinization using three washes of Histo-Clear (National Diagnostics, Atlanta, GA) for 5 min each, followed by two washes of a 50/50 mixture of absolute ethanol and Histo-Clear for 3 min each. Subsequently, the slides were gradually rehydrated in two washes of 100% (v/v) ethanol (3 min each), followed by one wash of 95% (v/v), 70% (v/v), 50% (v/v), and 0% (v/v) ethanol for 3 min each. The slides were then incubated in 0.5% Triton-X-100 (Millipore Sigma, Burlington, MA) in PBS for 5 min, followed by three washes with PBS. Afterward, the slides were blocked in a solution containing 20% goat serum and 0.3% Triton-X-100 in TBS for 2 h.

Primary antibodies targeting insulin and glucagon (Table 2) were applied to the slides in a solution containing 2% goat serum and 0.3% Triton-X-100 in TBS overnight at 4°C. The slides were then

washed three times with PBS and subsequently incubated with secondary antibodies in a solution containing 2% goat serum and 0.3% Triton-X-100 for 1 h. Following this, the solution was removed, and DAPI (1:1,000) in PBS was added for 5 min at room temperature. The slides were washed three times with PBS and mounted in Fluoromount-G™ Mounting Medium (Invitrogen).

Images were taken using an Axio Imager M2 microscope (Zeiss) and captured with a 40X objective. The number of glucagon and insulin positive cells per islet was counted for each mouse.

4.4.2 Spinal cord (SC)

Lumbar spinal cord sections were prepared for choline acetyltransferase (ChAT) staining of motor neurons. The slides were air-dried at room temperature for 30 min and then rinsed in TBS-T for 5 min. Samples were permeabilized in 0.3% Triton X-100 in PBS for 30 min, followed by blocking in 1x Power Block (BioGenex, Fremont, CA) for 20 min at room temperature. Subsequently, the samples were incubated with a goat anti-ChAT (details in Table 2) antibody at a dilution of 1:100 in 1% BSA and 0.3% Triton X-100 in PBS for 3 nights at 4°C.

After the initial antibody incubation, slides were washed twice for 10 min with TBS-T at room temperature. Following the washes, samples were then incubated with Alexa Fluor 555 donkey anti-goat IgG at a dilution of 1:200 in 10% donkey serum and 0.3% Triton X-100 in PBS for 2 h at room temperature in a humid chamber. Nuclei were counterstained with 4',6-diamidino-2-phenylindole (DAPI) at a dilution of 1:1000 in PBS for 5 min.

Finally, the slides were rinsed 3X for 10 min with TBS-T and mounted with Fluoromount-G™ Mounting Medium (Invitrogen). SC were examined under fluorescence using an Axio Imager M2 microscope (Zeiss) and imaged at 20X magnification for quantification, and at 63x for representative pictures. The number of ChAT-positive motor neurons with a diameter of ≥20 µm per ventral horn was recorded for 7-10 different sections per animal, each separated by at least 100 µm to prevent re-counting of the same motor neuron. An average number of motor neuron cell bodies per section was determined.

4.4.3 Neuromuscular Junction (NMJ)

To evaluate neuromuscular innervation, we performed immunohistochemistry using established protocols[26]. After euthanasia, the TVA muscles were promptly dissected and fixed in 4% paraformaldehyde (Electron Microscopy Science) in PBS for 15 min. Post-synaptic acetylcholine receptors (AChRs) were labeled for 10 min with alpha-bungarotoxin (aBTX) conjugated to Alexa Fluor 488. Subsequently, the muscles were blocked in 4% bovine serum albumin (BSA) and 1% Triton-X-100 in PBS for 30 min.

Following blocking, the muscles underwent overnight incubation with primary antibodies for neurofilament and synaptic vesicle protein 2 (refer to Table 2). Visualization of the labeled structures was achieved using DyLight-conjugated secondary antibodies. The muscles were then whole-mounted in Dako Fluorescent mounting media and imaged with a 20x objective on a Zeiss Axio Imager M1 microscope.

383 A minimum of three fields of view (FOV) were quantified per muscle. For each FOV, the
384 percentage of fully occupied endplates was noted. Fully occupied endplates were defined as motor
385 endplates completely covered by the presynaptic terminal labeled with synaptic vesicle protein 2
386 (SV2) and neurofilament (NF).
387
388 **Table 2. List of antibodies used.**
389

Application	*Antibody*	*Species*	*Dilution*	*Company (Catalog #)*
Western Blot	SMN	Mouse	1:2 500	BD Transduction (610647)
Western Blot	Alpha-tubulin	Rabbit	1:10 000	Abcam (ab4074)
Western Blot	Alpha-tubulin	Mouse	1:10 000	Sigma-Aldrich (CP06)
Western Blot	Heme oxygenase-1 (HO)	Rabbit	1:10 000	Abcam (ab68477)
Western Blot	P62	Mouse	1:1 000	Abcam (ab56416)
Western Blot	Transferrin	Rabbit	1:1 000	Abcam (ab82411)
Western Blot	Goat anti-mouse IR Dye 800 CW		1:5 000	LI-COR (925-32210)
Western Blot	Goat anti-mouse IR Dye 680 R		1:5 000	LI-COR (926-68070)
Western Blot	Goat anti-rabbit IR Dye 800 CW		1:5 000	LI-COR (925-32211)
Western Blot	Goat anti-rabbit IR Dye 680 R		1:5 000	LI-COR (926-68071)
IHC	ChAT	Goat	1:100	Millipore (AB144P)
IHC	Donkey anti-goat Alexa Fluor 555		1:200	Invitrogen (A21432)
IHC	TRITC conjugated bungarotoxin	N/A	1:1 000	Invitrogen (T1175)
IHC	Neurofilament (NF-M)	Mouse	1:100	(Developmental Studies Hybridoma Bank, P12839)
IHC	Synaptic vesicle glycoprotein 2A (SV2A)	Mouse	1:250	(Developmental Studies Hybridoma Bank, Q7L0J3)
IHC	Goat anti-mouse Alexa Fluor 488		1:250	Invitrogen (A11001)
IHC	Glucagon	Mouse	1:200	Abcam (ab10988)
IHC	Insulin	Rabbit	1:50	Abcam (ab181547)

IHC	Goat anti-mouse Alexa Fluor 555	1:500	Invitrogen (A21422)
IHC	Goat anti-rabbit Alexa Fluor 488	1:500	Invitrogen (A11034)

390 *4.5 Muscle fiber analysis*
391
392 Muscle fiber analysis was performed using ImageJ software (version 2.9.0/1.53t). A total of one
393 hundred fibers were evaluated per animal, covering various regions of the muscle section to ensure
394 good representation. The area of each fiber was measured in square micrometers (μm^2) to compute
395 both the average and distribution of fiber sizes for each animal.
396
397 *4.6 Glucose levels*
398
399 Non-fasting blood glucose concentrations were assessed using a OneTouch Ultra2 Blood Glucose
400 Test Strips (LifeScan Europe GmbH, Zug, Switzerland) immediately following blood collection.
401 Approximately 2 µL of blood was applied to the test strip for glucose concentration measurement.
402
403 *4.7 ELISA for Insulin-like Growth Factor I (IGF-1)*
404
405 The concentration of IGF-1 in the liver was quantified using the Mouse/Rat IGF-I/IGF1
406 Quantikine ELISA Kit (MG100, R&D Systems, Inc., Minneapolis, MN, USA). Liver protein
407 lysates were diluted at a ratio of 1:6 in calibrator diluent and the assay was performed following
408 the manufacturer's instructions.
409
410 *4.8 Triglycerides quantification*
411
412 Liver tissues from P19 mice were promptly dissected and flash frozen. Subsequently, triglyceride
413 analysis was conducted at the Vanderbilt Mouse Metabolic Phenotyping Center, employing
414 established protocols previously utilized by our team[18].
415
416 *4.9 Motor function, weight, and survival assessments*
417
418 Motor function, weight, and survival were assessed according to established protocols[36]. Spinal
419 reflexes were evaluated using the righting reflex test, while motor balance and coordination were
420 evaluated with the pen test. Additionally, muscle strength was measured using the inverted mesh
421 grip test (see Fig. 9A). The righting reflex test was conducted from P7 to P13, the inverted mesh
422 grip test from P13 to P25, and the pen test from P19 to P25. Assessments were performed every
423 two days. A maximum duration of 30 sec for the pen test and 60 sec for the inverted mesh grip
424 represented the established threshold. Three consecutive measurements were obtained, and their
425 average was recorded for subsequent analysis. Weight was measured every two days starting at
426 day 7 until day 30, and then weekly until day 60. Animal welfare was monitored throughout the
427 60-day period during weight measurements.
428
429 *4.10 Statistical analysis*
430

Survival data were visualized using Kaplan-Meier survival curves, and intergroup differences were evaluated using the Mantel-Cox test. Brown-Forsythe and Welch ANOVA were employed to compare three or more sets of unpaired measurements, given the mosaic-like outcome observed in the $Alb^{Cre/+};Smn^{2B/F7}$ model, where assumptions of equal variances were not tenable. Two-way ANOVA, followed by Šídák's method for multiple comparisons, was utilized to assess the influence of two factors on a response. Statistical analyses were conducted using GraphPad Prism V.10.2.1 (GraphPad Prism Software, San Diego, CA), with significance set at $P < 0.05$. Data were presented as mean ± standard error of the mean. Sample sizes (n) are provided in figure legends, indicating the number of biological replicates analyzed, with each data point corresponding to an individual mouse from at least two different litters. Detailed statistical information is outlined in the respective figure legends, where statistical significance is indicated by *, $p < 0.05$; **, $p < 0.01$; ***, $p < 0.001$.

Data sharing

All authors had access to the study data and reviewed and approved the final manuscript. All data associated with this study are available in the main text or supplementary materials. Raw data can be provided upon request.

Acknowledgements

This work was supported by Muscular Dystrophy Association (USA) [grant number 963652 to R.K.]; the Canadian Institutes of Health Research [grant number PJT-186300 to R.K.]; and the University of Ottawa Brain and Mind Institute TRIMS Award to MMAA.

Declaration of interests

The authors disclose no conflicts of interest. The funders mentioned above were not involved in the study design, data collection and analysis, decision to publish, or manuscript preparation.

References

1 Lefebvre, S. *et al.* Identification and characterization of a spinal muscular atrophy-determining gene. *Cell* **80**, 155-165 (1995).

2 Lefebvre, S. *et al.* Correlation between severity and SMN protein level in spinal muscular atrophy. *Nat Genet* **16**, 265-269 (1997).

3 Crawford, T. O. & Pardo, C. A. The Neurobiology of Childhood Spinal Muscular Atrophy. *Neurobiology of Disease* **3**, 97-110 (1996).

4 Finkel, R. S. *et al.* Treatment of infantile-onset spinal muscular atrophy with nusinersen: a phase 2, open-label, dose-escalation study. *Lancet* **388**, 3017-3026 (2016). https://doi.org:10.1016/S0140-6736(16)31408-8

5 Lorson, C. L., Hahnen, E., Androphy, E. J. & Wirth, B. A single nucleotide in the SMN gene regulates splicing and is responsible for spinal muscular atrophy. *Proc Natl Acad Sci U S A* **96**, 6307-6311 (1999).

6 Feldkotter, M., Schwarzer, V., Wirth, R., Wienker, T. F. & Wirth, B. Quantitative analyses of SMN1 and SMN2 based on real-time lightCycler PCR: fast and highly

476 reliable carrier testing and prediction of severity of spinal muscular atrophy. *Am J Hum*
477 *Genet* **70**, 358-368 (2002). https://doi.org:10.1086/338627
478 7 Schrank, B. *et al.* Inactivation of the survival motor neuron gene, a candidate gene for
479 human spinal muscular atrophy, leads to massive cell death in early mouse embryos.
480 *Proc Natl Acad Sci U S A* **94**, 9920-9925 (1997).
481 8 Vitte, J. M. *et al.* Deletion of murine Smn exon 7 directed to liver leads to severe defect
482 of liver development associated with iron overload. *Am J Pathol* **165**, 1731-1741 (2004).
483 https://doi.org:10.1016/S0002-9440(10)63428-1
484 9 Bowerman, M. *et al.* Defects in pancreatic development and glucose metabolism in
485 SMN-depleted mice independent of canonical spinal muscular atrophy neuromuscular
486 pathology. *Hum Mol Genet* **23**, 3432-3444 (2014). https://doi.org:10.1093/hmg/ddu052
487 10 Bowerman, M., Murray, L. M., Beauvais, A., Pinheiro, B. & Kothary, R. A critical smn
488 threshold in mice dictates onset of an intermediate spinal muscular atrophy phenotype
489 associated with a distinct neuromuscular junction pathology. *Neuromuscul Disord* **22**,
490 263-276 (2012). https://doi.org:S0960-8966(11)01345-9 [pii] 10.1016/j.nmd.2011.09.007
491 11 Bowerman, M. *et al.* Glucose metabolism and pancreatic defects in spinal muscular
492 atrophy. *Ann Neurol* **72**, 256-268 (2012).
493 12 Deguise, M. O. *et al.* Abnormal fatty acid metabolism is a core component of spinal
494 muscular atrophy. *Ann Clin Transl Neurol* **6**, 1519-1532 (2019).
495 https://doi.org:10.1002/acn3.50855
496 13 Chiriboga, C. A. Nusinersen for the treatment of spinal muscular atrophy. *Expert Rev*
497 *Neurother* **17**, 955-962 (2017). https://doi.org:10.1080/14737175.2017.1364159
498 14 McMillan, H. J. *et al.* Onasemnogene abeparvovec for the treatment of spinal muscular
499 atrophy. *Expert Opin Biol Ther* **22**, 1075-1090 (2022).
500 https://doi.org:10.1080/14712598.2022.2066471
501 15 Crawford, T. O., Sladky, J. T., Hurko, O., Besner-Johnston, A. & Kelley, R. I. Abnormal
502 fatty acid metabolism in childhood spinal muscular atrophy. *Ann Neurol* **45**, 337-343
503 (1999).
504 16 Deguise, M. O., Chehade, L. & Kothary, R. Metabolic Dysfunction in Spinal Muscular
505 Atrophy. *Int J Mol Sci* **22** (2021). https://doi.org:10.3390/ijms22115913
506 17 Deguise, M. O., Chehade, L., Tierney, A., Beauvais, A. & Kothary, R. Low fat diets
507 increase survival of a mouse model of spinal muscular atrophy. *Ann Clin Transl Neurol*
508 **6**, 2340-2346 (2019). https://doi.org:10.1002/acn3.50920
509 18 Deguise, M. O. *et al.* SMN Depleted Mice Offer a Robust and Rapid Onset Model of
510 Nonalcoholic Fatty Liver Disease. *Cell Mol Gastroenterol Hepatol* **12**, 354-377 e353
511 (2021). https://doi.org:10.1016/j.jcmgh.2021.01.019
512 19 Trefts, E., Gannon, M. & Wasserman, D. H. The liver. *Curr Biol* **27**, R1147-R1151
513 (2017). https://doi.org:10.1016/j.cub.2017.09.019
514 20 DiDonato, C. J. *et al.* Regulation of murine survival motor neuron (Smn) protein levels
515 by modifying Smn exon 7 splicing. *Hum Mol Genet* **10**, 2727-2736. (2001).
516 21 Hammond, S. M. *et al.* Mouse survival motor neuron alleles that mimic SMN2 splicing
517 and are inducible rescue embryonic lethality early in development but not late. *PLoS One*
518 **5**, e15887 (2010). https://doi.org:10.1371/journal.pone.0015887
519 22 Postic, C. *et al.* Dual roles for glucokinase in glucose homeostasis as determined by liver
520 and pancreatic beta cell-specific gene knock-outs using Cre recombinase. *J Biol Chem*
521 **274**, 305-315 (1999). https://doi.org:10.1074/jbc.274.1.305

23 Frugier, T. *et al.* Nuclear targeting defect of SMN lacking the C-terminus in a mouse model of spinal muscular atrophy. *Hum Mol Genet* **9**, 849-858 (2000).

24 Eshraghi, M., McFall, E., Gibeault, S. & Kothary, R. Effect of genetic background on the phenotype of the Smn2B/- mouse model of spinal muscular atrophy. *Hum Mol Genet* **25**, 4494-4506 (2016). https://doi.org:10.1093/hmg/ddw278

25 Reilly, A., Yaworski, R., Beauvais, A., Schneider, B. L. & Kothary, R. Long term peripheral AAV9-SMN gene therapy promotes survival in a mouse model of spinal muscular atrophy. *Hum Mol Genet* **33**, 510-519 (2024). https://doi.org:10.1093/hmg/ddad202

26 Reilly, A. *et al.* Central and peripheral delivered AAV9-SMN are both efficient but target different pathomechanisms in a mouse model of spinal muscular atrophy. *Gene Ther* **29**, 544-554 (2022). https://doi.org:10.1038/s41434-022-00338-1

27 Deguise, M. O. *et al.* Differential induction of muscle atrophy pathways in two mouse models of spinal muscular atrophy. *Sci Rep* **6**, 28846 (2016). https://doi.org:10.1038/srep28846

28 Deguise, M. O. *et al.* Motor transmission defects with sex differences in a new mouse model of mild spinal muscular atrophy. *EBioMedicine* **55**, 102750 (2020). https://doi.org:10.1016/j.ebiom.2020.102750

29 Gavrilina, T. O. *et al.* Neuronal SMN expression corrects spinal muscular atrophy in severe SMA mice while muscle-specific SMN expression has no phenotypic effect. *Hum Mol Genet* **17**, 1063-1075 (2008).

30 Murray, L. M., Beauvais, A., Bhanot, K. & Kothary, R. Defects in neuromuscular junction remodelling in the *Smn2B/-* mouse model of spinal muscular atrophy. *Neurobiology of Disease* **49C**, 57-67 (2012).

31 Murray, L. M., Beauvais, A., Gibeault, S., Courtney, N. L. & Kothary, R. Transcriptional profiling of differentially vulnerable motor neurons at pre-symptomatic stage in the Smn (2b/-) mouse model of spinal muscular atrophy. *Acta Neuropathol Commun* **3**, 55 (2015). https://doi.org:10.1186/s40478-015-0231-1

32 Shababi, M., Lorson, C. L. & Rudnik-Schoneborn, S. S. Spinal muscular atrophy: a motor neuron disorder or a multi-organ disease? *J Anat* **224**, 15-28 (2014). https://doi.org:10.1111/joa.12083

33 Lorson, C. L., Rindt, H. & Shababi, M. Spinal muscular atrophy: mechanisms and therapeutic strategies. *Hum Mol Genet* **19**, R111-118 (2010). https://doi.org:10.1093/hmg/ddq147

34 Hua, Y. *et al.* Peripheral SMN restoration is essential for long-term rescue of a severe spinal muscular atrophy mouse model. *Nature* **478**, 123-126 (2011). https://doi.org:nature10485 [pii] 10.1038/nature10485

35 Mercuri, E., Sumner, C. J., Muntoni, F., Darras, B. T. & Finkel, R. S. Spinal muscular atrophy. *Nat Rev Dis Primers* **8**, 52 (2022). https://doi.org:10.1038/s41572-022-00380-8

36 Chehade, L. *et al.* Suppression of the necroptotic cell death pathways improves survival in Smn (2B/-) mice. *Front Cell Neurosci* **16**, 972029 (2022). https://doi.org:10.3389/fncel.2022.972029

37 Hua, Y. *et al.* Motor neuron cell-nonautonomous rescue of spinal muscular atrophy phenotypes in mild and severe transgenic mouse models. *Genes Dev* **29**, 288-297 (2015). https://doi.org:10.1101/gad.256644.114

567 38 Muckenthaler, M. U., Rivella, S., Hentze, M. W. & Galy, B. A Red Carpet for Iron
568 Metabolism. *Cell* **168**, 344-361 (2017). https://doi.org:10.1016/j.cell.2016.12.034
569 39 Manley, S., Williams, J. A. & Ding, W. X. Role of p62/SQSTM1 in liver physiology and
570 pathogenesis. *Exp Biol Med (Maywood)* **238**, 525-538 (2013).
571 https://doi.org:10.1177/1535370213489446
572 40 Hribal, M. L. *et al.* Insulin-like growth factor-I, inflammatory proteins, and fibrosis in
573 subjects with nonalcoholic fatty liver disease. *J Clin Endocrinol Metab* **98**, E304-308
574 (2013). https://doi.org:10.1210/jc.2012-3290
575 41 Ichikawa, T. *et al.* Role of growth hormone, insulin-like growth factor 1 and insulin-like
576 growth factor-binding protein 3 in development of non-alcoholic fatty liver disease.
577 *Hepatol Int* **1**, 287-294 (2007). https://doi.org:10.1007/s12072-007-9007-4
578 42 Heffner, C. S. *et al.* Supporting conditional mouse mutagenesis with a comprehensive cre
579 characterization resource. *Nat Commun* **3**, 1218 (2012).
580 https://doi.org:10.1038/ncomms2186
581 43 Cifuentes-Diaz, C. *et al.* Deletion of murine SMN exon 7 directed to skeletal muscle
582 leads to severe muscular dystrophy. *J Cell Biol* **152**, 1107-1114. (2001).
583 44 Cifuentes-Diaz, C. *et al.* Neurofilament accumulation at the motor endplate and lack of
584 axonal sprouting in a spinal muscular atrophy mouse model. *Hum Mol Genet* **11**, 1439-
585 1447. (2002).

586 **Figure subtitles**
587
588 1. **Generation of liver specific SMN depleted mice.** A. Schematic representation of the
589 breeding scheme to generate liver specific SMN depletion. In these mice, the *Smn* gene carries
590 one Smn^{2B} allele that harbors a three-nucleotide switch in exon 7, and one *Smn* allele whose
591 exon 7 is floxed by loxP sites (Smn^{F7}). The *Alb-Cre* transgene has also been crossed into this
592 background to provide liver-specific expression of the Cre recombinase. B. Littermate controls
593 do not harbor Cre recombinase but do carry one Smn^{2B} allele and are thus used as heterozygous
594 controls. C. Upon crossing $Alb^{Cre/+};Smn^{F7/+}$ with $Smn^{2B/F7}$ animals, Cre recombination will
595 induce specific excision of exon 7 in the liver, leading to reduced SMN protein production
596 only in the liver.
597
598 2. **Liver-specific SMN depletion in $Alb^{Cre/+};Smn^{2B/F7}$ mice.** A–E. Immunoblots were performed
599 to assess SMN protein levels in various tissues from $Smn^{2B/+}$, $Smn^{2B/-}$, +/+;$Smn^{2B/F7}$, and
600 $Alb^{Cre/+};Smn^{2B/F7}$ mice at P19. Membranes were probed for SMN and then reprobed for α-
601 tubulin (loading control). A'-E'. Bar graphs show quantification of SMN protein levels in the
602 liver (A'), brain (B'), muscle (C'), spinal cord and pancreas (E'), normalized to α-tubulin.
603 $n \geq 3$, mean ± SEM. Statistical significance indicated by $*p < 0.05$, $**p < 0.01$ or p values,
604 following Brown-Forsythe and Welch ANOVA.
605
606 3. **Impact of liver specific SMN depletion in hepatocyte morphology and lipid accumulation.**
607 A. Representative images of H&E (top row, scale bar 100 μm) and Oil Red-O (bottom row,
608 scale bar 50 μm) stained liver sections from $Smn^{2B/+}$, $Smn^{2B/-}$, +/+;$Smn^{2B/F7}$, and
609 $Alb^{Cre/+};Smn^{2B/F7}$ mice at P19. B. Bar graph shows quantification of liver triglycerides. $n \geq 3$,
610 mean ± SEM. Statistical significance indicated by $*p < 0.05$, $**p < 0.01$, following Brown-
611 Forsythe and Welch ANOVA.
612
613 4. **Levels of key proteins involved in liver homeostatic function are unchanged in liver-**
614 **specific SMN-depleted mice.** A-C. Immunoblots were performed to assess heme oxygenase
615 (HO, A-A'), transferrin (B-B') and P62 (C-C') protein levels in the liver. α-tubulin was used
616 as a loading control. A'-C' Bar graphs show quantification of HO (A'), transferrin (B'), and
617 P62 (C') levels. D. Bar graph depicts quantification of liver IGF-1. $n \geq 3$, mean ± SEM.
618 Statistical significance indicated by $*p < 0.05$, $***p < 0.001$, following Brown-Forsythe and
619 Welch ANOVA.
620
621 5. **Contribution of liver specific SMN depletion to pancreatic pathology.** A. Representative
622 immunofluorescent images of pancreatic islets stained for glucagon (red) and insulin (green)
623 from $Smn^{2B/+}$, $Smn^{2B/-}$, +/+;$Smn^{2B/F7}$, and $Alb^{Cre/+};Smn^{2B/F7}$ mice at P19. Scale bar 50 μm. B-C.
624 Bar graphs show quantification of insulin (B) and glucagon (C) positive cells relative to the
625 total number of DAPI positive cells within the pancreatic islet. D. Bar graph depicts non-
626 fasting blood glucose levels from P19 mice across different genotypes. $n \geq 3$, mean ± SEM.
627 Statistical significance indicated by $*p < 0.05$, $**p < 0.01$, $***p < 0.001$, following Brown-
628 Forsythe and Welch ANOVA.
629
630 6. **Impact of liver specific SMN depletion on motor neuron cell body numbers.** A.
631 Representative images of lumbar spinal cord anterior horns stained for ChAT (red) and DAPI

632 (blue) from *Smn*$^{2B/+}$, *Smn*$^{2B/-}$, +/+;*Smn*$^{2B/F7}$, and *Alb*$^{Cre/+}$;*Smn*$^{2B/F7}$ mice at P19. B. Bar graph
633 shows quantification of motor neuron cell body numbers. $n \geq 3$, mean ± SEM. Statistical
634 significance indicated by $^{**}p < 0.01$, $^{***}p < 0.001$, following Brown-Forsythe and Welch
635 ANOVA. Scale bar = 50 μm.
636
637 **7. Impact of liver specific SMN depletion on neuromuscular junction pathology.** A.
638 Representative images of *transversus abdominis* (TVA) muscle stained with bungarotoxin
639 (red), neurofilament (NF) (green) and synaptic vesicle protein 2 (green) from *Smn*$^{2B/+}$, *Smn*$^{2B/-}$
640 , +/+;*Smn*$^{2B/F7}$, and *Alb*$^{Cre/+}$;*Smn*$^{2B/F7}$ mice at P19. *Depicts occupied endplate, whereas
641 **depicts normal neurofilament distribution; arrowheads show NF accumulation and arrows
642 show unoccupied endplate/denervation. B-C. Bar graphs show quantification of neurofilament
643 accumulation (B) and endplate occupancy (C). $n = 3$, mean ± SEM. Statistical significance
644 indicated by $^{**}p < 0.01$, $^{***}p < 0.001$, following Brown-Forsythe and Welch ANOVA. Scale
645 bar = 50 μm.
646
647 **8. Impact of liver specific SMN depletion on muscle fiber size and distribution.** A.
648 Representative images of H&E-stained *tibialis anterior* muscle sections from *Smn*$^{2B/+}$, *Smn*$^{2B/-}$
649 , +/+;*Smn*$^{2B/F7}$, and *Alb*$^{Cre/+}$;*Smn*$^{2B/F7}$ mice at P19. B. Bar graph shows quantification of muscle
650 fiber cross-sectional area. C. Graph demonstrating frequency of muscle fiber size across
651 different genotypes. $n \geq 3$, mean ± SEM. Statistical significance indicated by $^{**}p < 0.01$,
652 following Brown-Forsythe and Welch ANOVA. Scale bar = 20 μm.
653
654 **9. Impact of liver specific SMN depletion on motor function**. A. Schematic representation of
655 experimental design. The righting reflex test was conducted from P7 to P13, the inverted mesh
656 grip test from P13 to P25, and the pen test from P19 to P25. Assessments were performed every
657 two days. Weight was measured every two days until day 30, and then weekly until day 60.
658 Animal welfare was monitored throughout the 60-day period during weight measurements. B.
659 Kaplan–Meier survival curve comparing *Alb*$^{Cre/+}$;*Smn*$^{2B/F7}$ and +/+;*Smn*$^{2B/F7}$ mice up to 60
660 days. C-F. Graphs show weight (C), righting reflex (D), inverted mesh grip (E) and pen test
661 (F). n = 5 per genotype, mean ± SEM. B: Kaplan–Meier survival analysis; C-F: two-way
662 ANOVA, followed by Šídák's method.
663
664
665
666
667

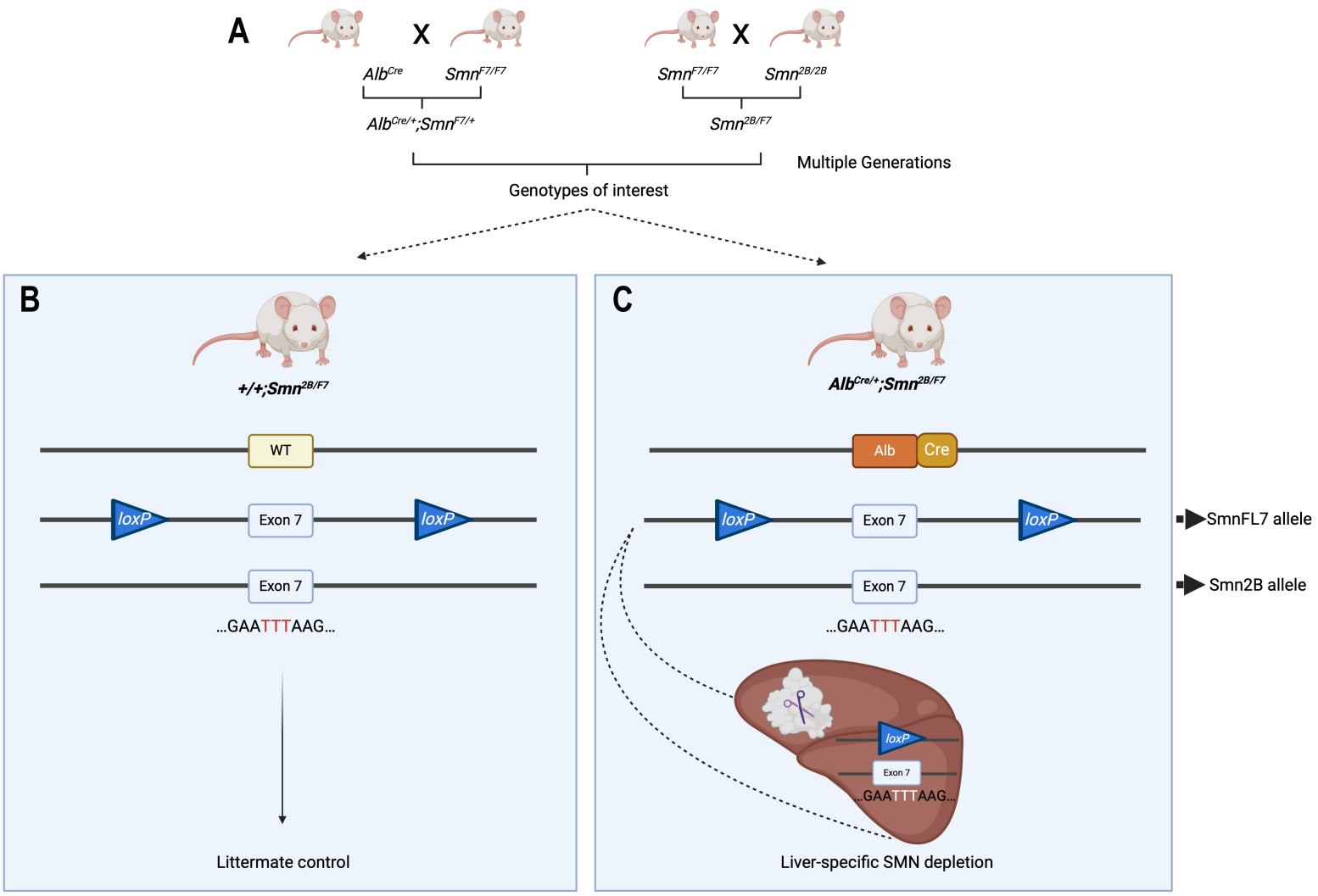
A
X
X
Alb^Cre
Smn^F7/F7
Smn^F7/F7
Smn^2B/2B
Alb^Cre/+;Smn^F7/+
Smn^2B/F7
Multiple Generations
Genotypes of interest
B
+/+;Smn^2B/F7
WT
loxP
Exon 7
loxP
Exon 7
...GAATTTAAG...
Littermate control
C
Alb^Cre/+;Smn^2B/F7
Alb
Cre
loxP
Exon 7
loxP
SmnFL7 allele
Exon 7
Smn2B allele
...GAATTTAAG...
loxP
Exon 7
...GAATTTAAG...
Liver-specific SMN depletion

Figure 1

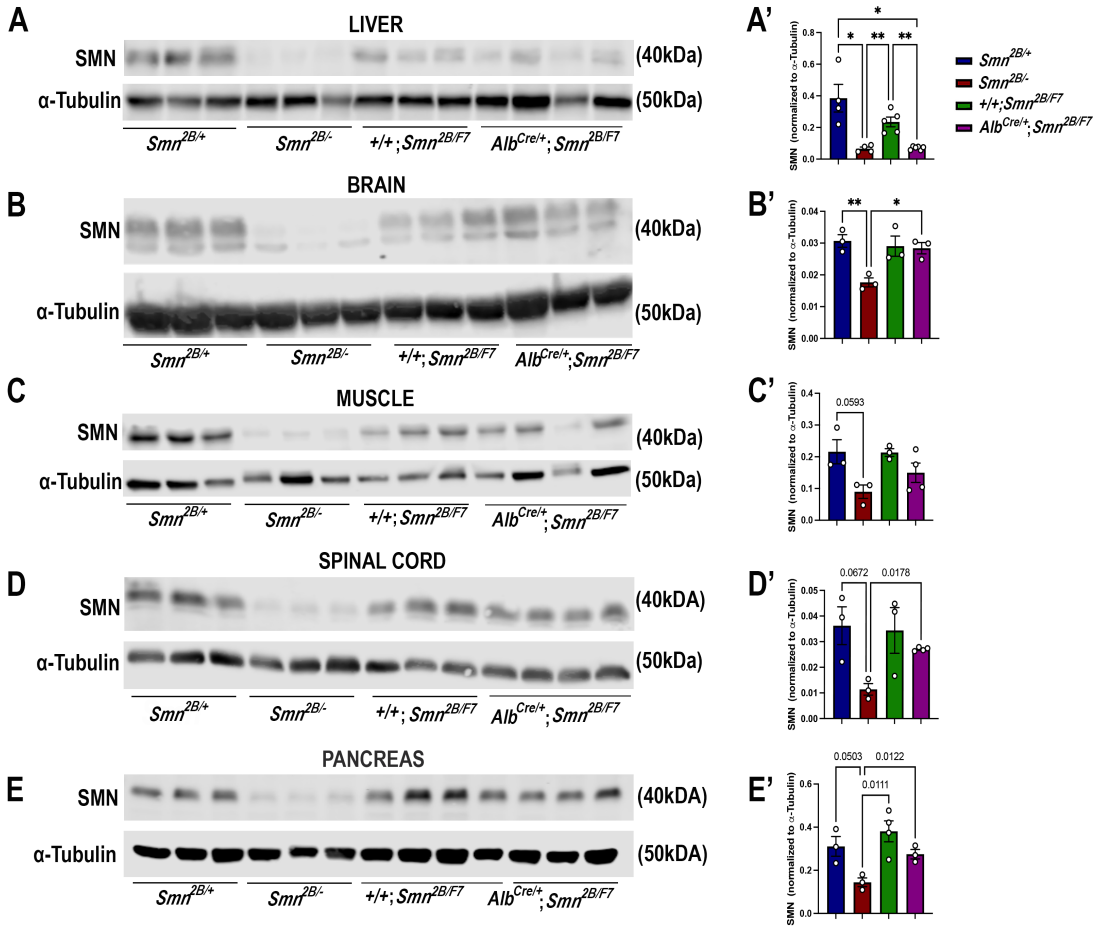
A
LIVER
SMN
α-Tubulin
(40kDa)
(50kDa)
Smn2B/+
Smn2B/-
+/+;Smn2B/F7
AlbCre/+;Smn2B/F7
A'
SMN (normalized to α-Tubulin)
B
BRAIN
B'
C
MUSCLE
C'
0.0593
D
SPINAL CORD
(40kDA)
D'
0.0672
0.0178
E
PANCREAS
E'
0.0503
0.0122
0.0111

Figure 2

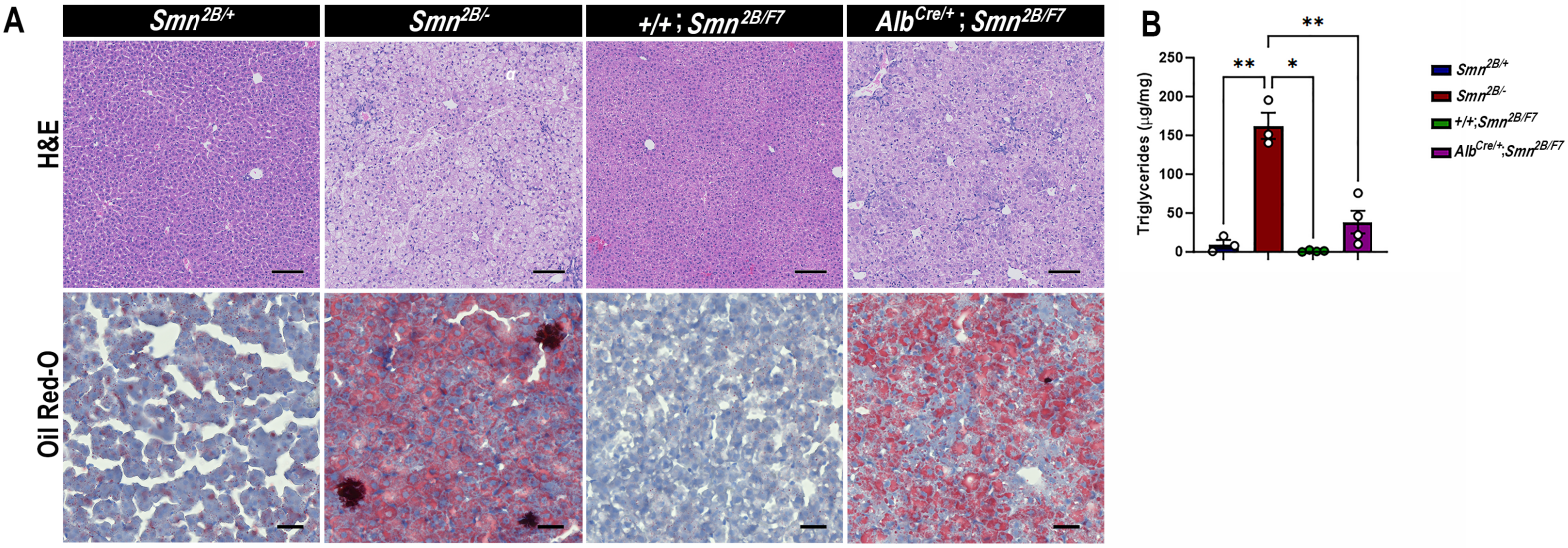
A
Smn2B/+
Smn2B/-
+/+ ; Smn2B/F7
AlbCre/+ ; Smn2B/F7
H&E
Oil Red-O
B
Triglycerides (µg/mg)
250
200
150
100
50
0
**
*
**
Smn2B/+
Smn2B/-
+/+;Smn2B/F7
AlbCre/+;Smn2B/F7

Figure 3

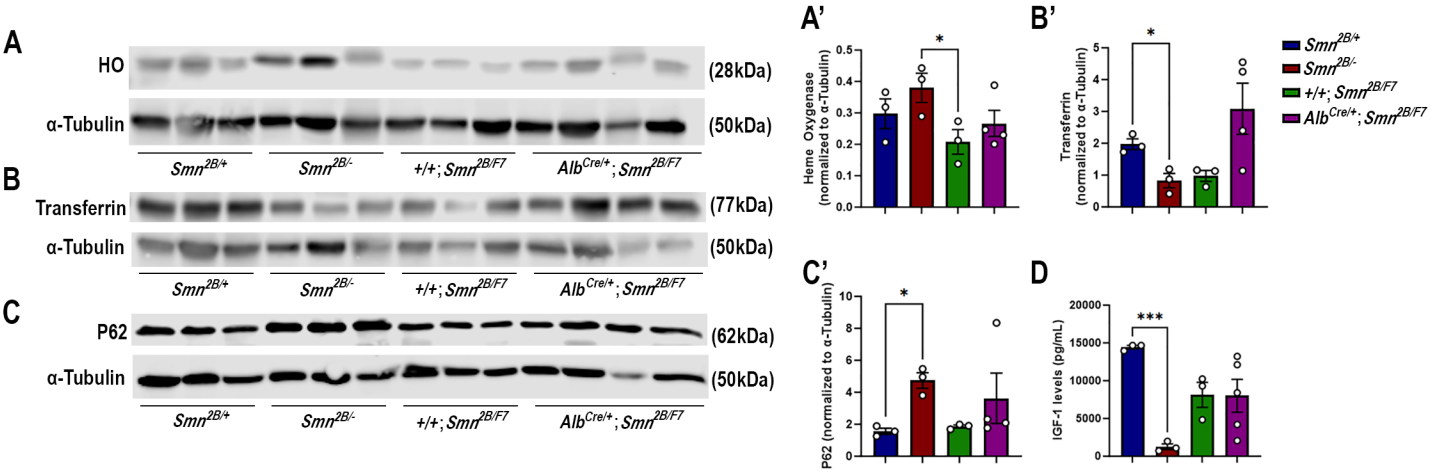
A
HO
(28kDa)
α-Tubulin
(50kDa)
Smn2B/+
Smn2B/-
+/+; Smn2B/F7
AlbCre/+; Smn2B/F7
B
Transferrin
(77kDa)
α-Tubulin
(50kDa)
C
P62
(62kDa)
α-Tubulin
(50kDa)
A'
Heme Oxygenase (normalized to α-Tubulin)
B'
Transferrin (normalized to α-Tubulin)
C'
P62 (normalized to α-Tubulin)
D
IGF-1 levels (pg/mL)
*
***

Figure 4

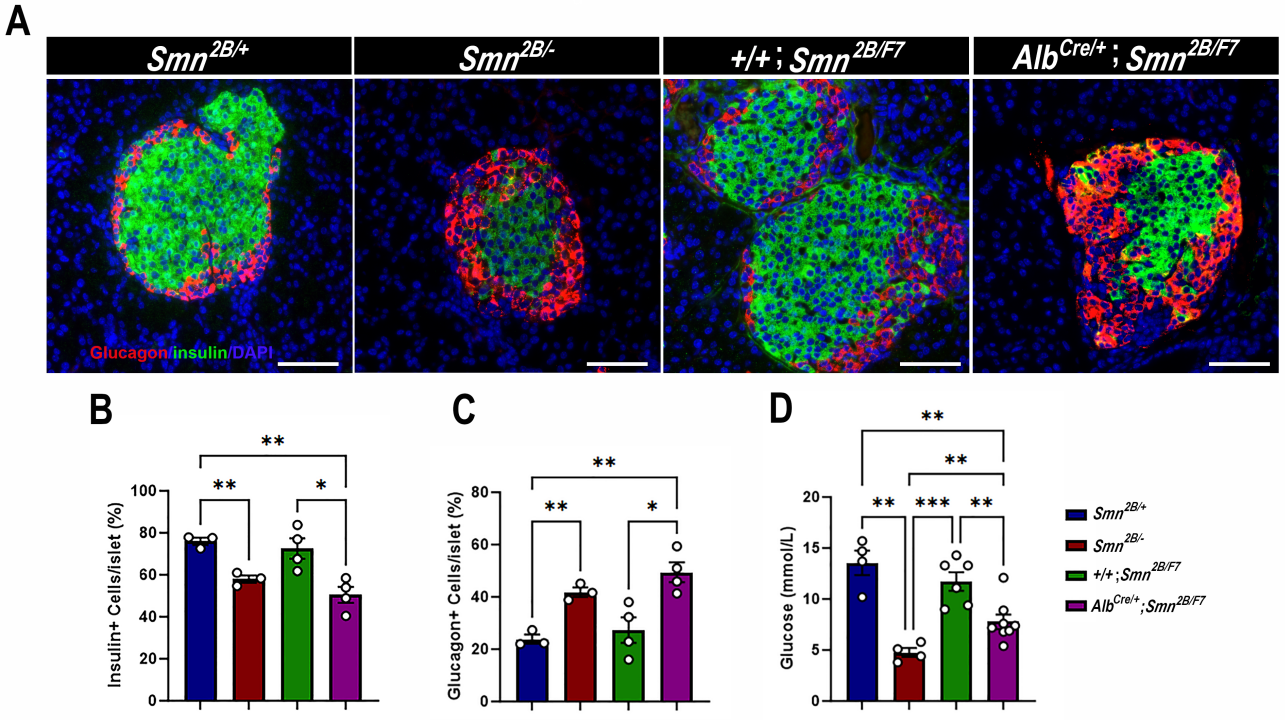
A
Smn2B/+
Smn2B/-
+/+;Smn2B/F7
AlbCre/+;Smn2B/F7
Glucagon/insulin/DAPI
B
Insulin+ Cells/Islet (%)
C
Glucagon+ Cells/Islet (%)
D
Glucose (mmol/L)
Smn2B/+
Smn2B/-
+/+;Smn2B/F7
AlbCre/+;Smn2B/F7

Figure 5

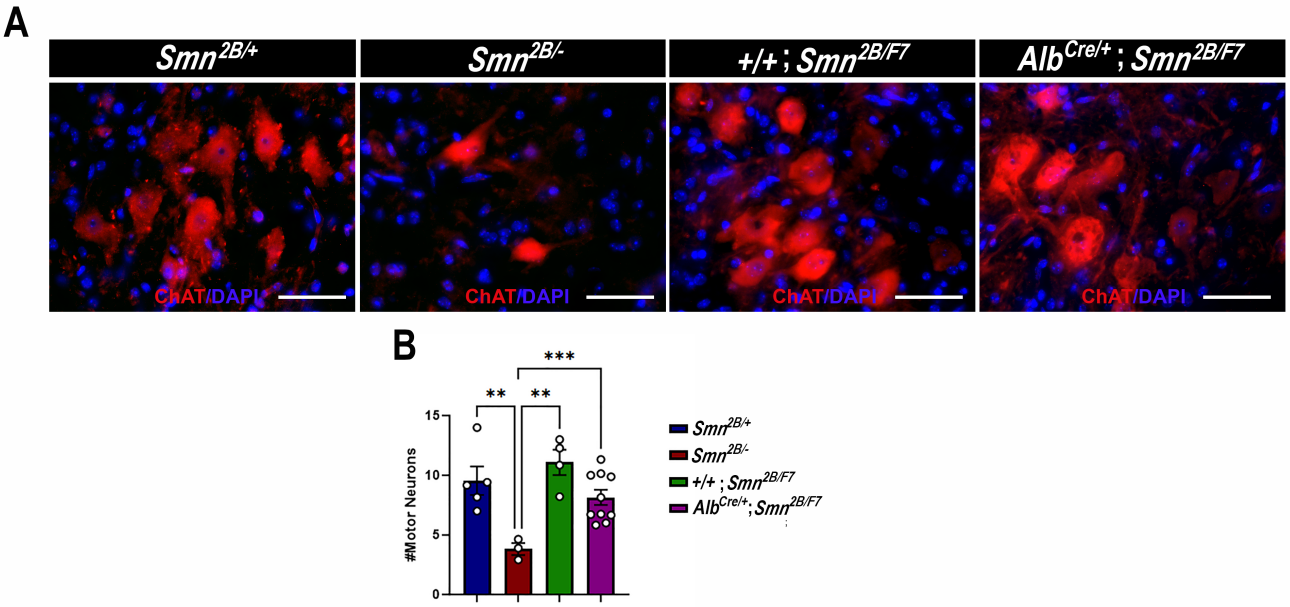
A
Smn2B/+
Smn2B/-
+/+ ; Smn2B/F7
AlbCre/+ ; Smn2B/F7
ChAT/DAPI
ChAT/DAPI
ChAT/DAPI
ChAT/DAPI
B
***
**
**
#Motor Neurons
15
10
5
0
Smn2B/+
Smn2B/-
+/+ ; Smn2B/F7
AlbCre/+; Smn2B/F7

Figure 6

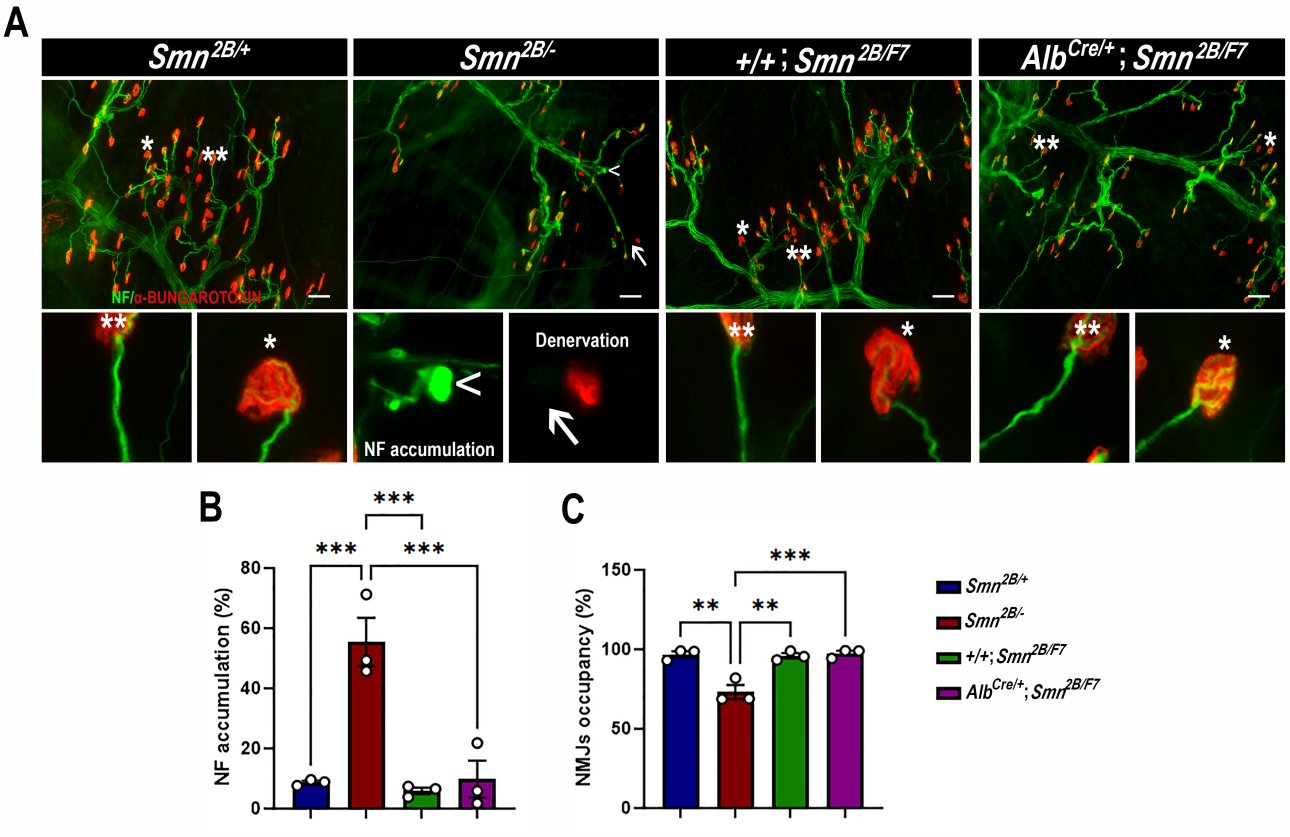
A
Smn2B/+
Smn2B/-
+/+; Smn2B/F7
AlbCre/+; Smn2B/F7
NF/α-BUNGAROTOXIN
Denervation
NF accumulation
B
NF accumulation (%)
C
NMJs occupancy (%)
Smn2B/+
Smn2B/-
+/+; Smn2B/F7
AlbCre/+; Smn2B/F7

Figure 7

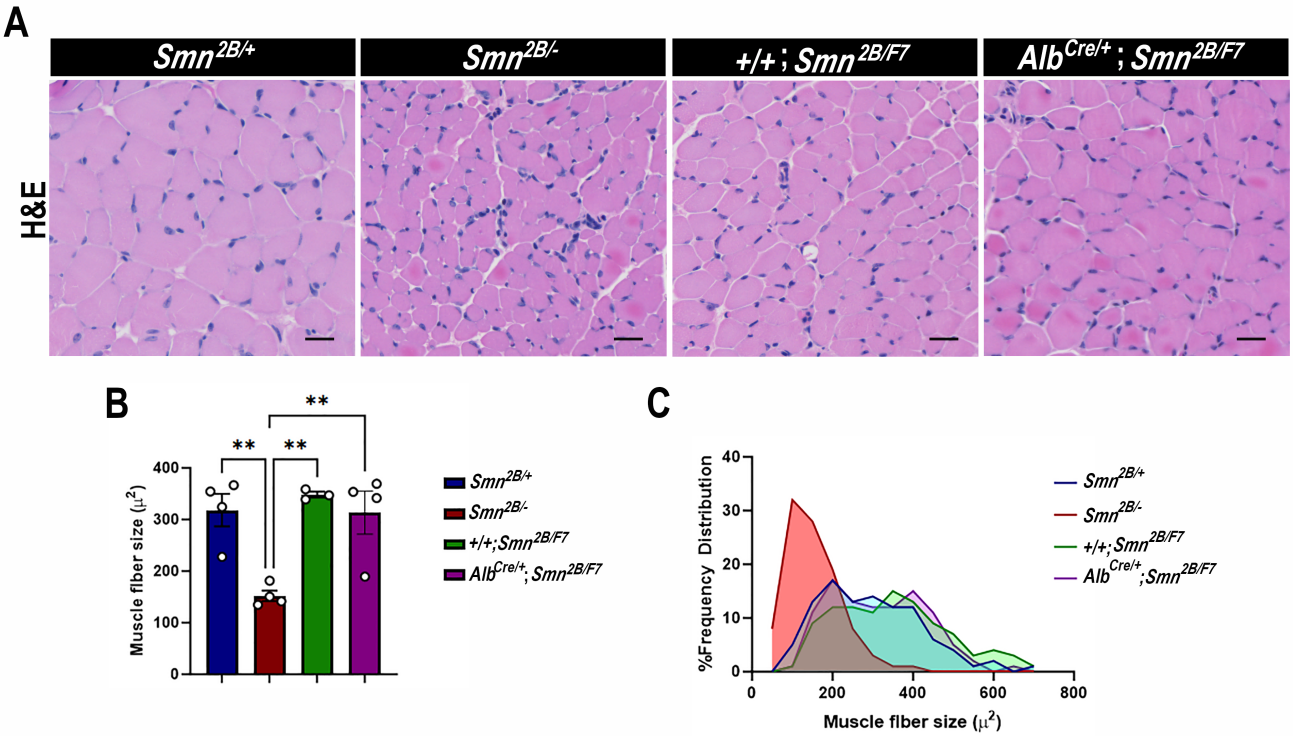
A
Smn2B/+
Smn2B/-
+/+; Smn2B/F7
AlbCre/+; Smn2B/F7
H&E
B
**
**
**
Muscle fiber size (μ2)
400
300
200
100
0
Smn2B/+
Smn2B/-
+/+;Smn2B/F7
AlbCre/+; Smn2B/F7
C
%Frequency Distribution
40
30
20
10
0
0
200
400
600
800
Muscle fiber size (μ2)
Smn2B/+
Smn2B/-
+/+;Smn2B/F7
AlbCre/+;Smn2B/F7

Figure 8

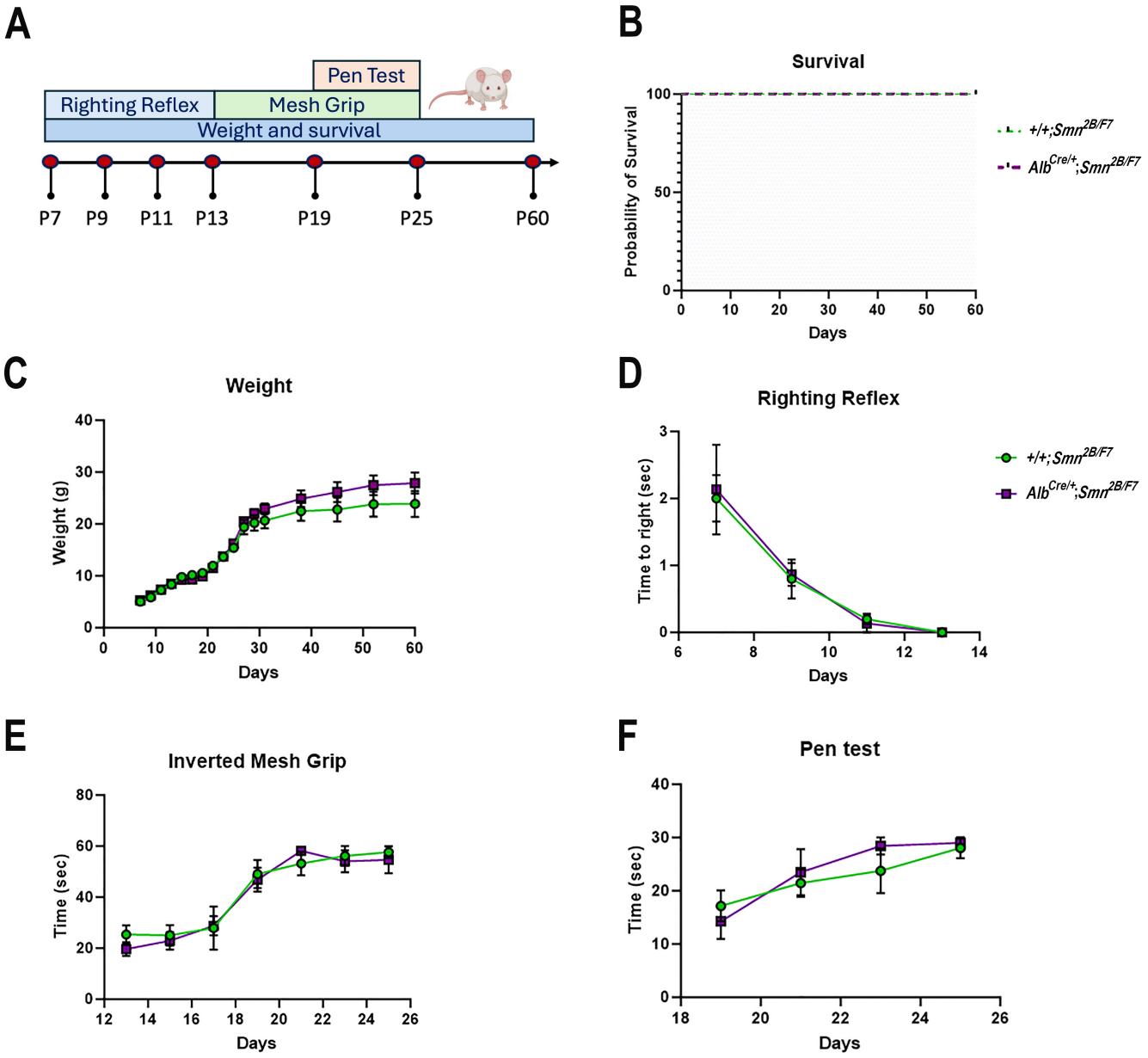
A
Pen Test
Righting Reflex
Mesh Grip
Weight and survival
P7
P9
P11
P13
P19
P25
P60
B
Survival
Probability of Survival
Days
+/+;Smn2B/F7
AlbCre/+;Smn2B/F7
C
Weight
Weight (g)
Days
D
Righting Reflex
Time to right (sec)
Days
+/+;Smn2B/F7
AlbCre/+;Smn2B/F7
E
Inverted Mesh Grip
Time (sec)
Days
F
Pen test
Time (sec)
Days

Figure 9